
Gaussian Splatting Lucas-Kanade

Liuyue Xie^{1*}, Joel Julin¹, Koichiro Niinuma², László A. Jeni¹

¹Carnegie Mellon University, ²Fujitsu Research of America,
{liuyue@andrew.jjulin@andrew.,laszlojeni@jcmu.edu, kniinuma@fujitsu.com

Abstract

Reconstructing dynamic 3D scenes from 2D images and generating diverse views over time presents a significant challenge due to the inherent complexity and temporal dynamics involved. While recent advancements in neural implicit models and dynamic Gaussian Splatting have shown promise, limitations persist, particularly in accurately capturing the underlying geometry of highly dynamic scenes. Some approaches address this by incorporating strong semantic and geometric priors through diffusion models. However, we explore a different avenue by investigating the potential of regularizing the native warp field within the dynamic Gaussian Splatting framework. Our method is grounded on the key intuition that an accurate warp field should produce continuous space-time motions. While enforcing the motion constraints on warp fields is non-trivial, we show that we can exploit knowledge innate to the forward warp field network to derive an analytical velocity field, then time integrate for scene flows to effectively constrain both the 2D motion and 3D positions of the Gaussians. This derived Lucas-Kanade style analytical regularization enables our method to achieve superior performance in reconstructing highly dynamic scenes, even under minimal camera movement, extending the boundaries of what existing dynamic Gaussian Splatting frameworks can achieve.

1 Introduction

The task of reconstructing dynamic 3D scenes from monocular video presents a significant challenge, particularly when constrained by limited camera movement. This limitation leads to a scarcity of parallax and epipolar constraints, which are crucial for accurately estimating scene structures [1, 2]. Implicit neural representation methods like NeRF have shown promise in mitigating this issue by modeling dynamic scenes using an implicit radiance field [3, 4, 5]. Explicit approaches like Gaussian splatting [6], while more efficient and often improves rendering quality, face additional hurdles. Gaussian splatting relies on an explicit representation of the scene using volumetric Gaussian functions. This necessitates a high degree of accuracy in geometric understanding to ensure proper scene depiction. Consequently, despite advancements in dynamic Gaussian splatting techniques, the requirement for diverse viewing angles to effectively constrain the placement of these Gaussians remains a limiting factor. This inherent limitation restricts their effectiveness for capturing scenes from static viewpoints or dealing with objects exhibiting rapid and complex movements.

Recent Gaussian splatting frameworks for modeling dynamic scenes commonly utilize a canonical Gaussian space as their foundation. This space is typically initialized using Structure from Motion (SfM) [7] point clouds, with which each Gaussian is assigned attributes that describe its position, orientation, and lighting-dependent color. This canonical space acts as a reference point from which deformations are applied to represent the dynamic scene at different time steps. The process of deforming the canonical space to depict the scene at a particular time step is achieved through a

*Corresponding Author

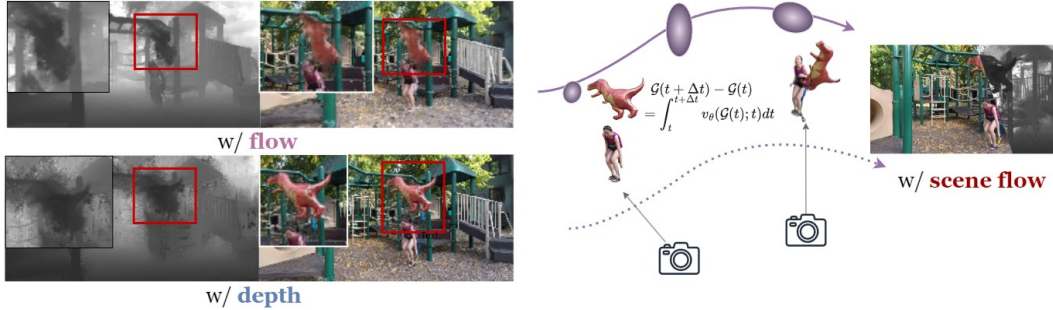


Figure 1: Data-driven depth and optical flow supervisions produce inaccurate geometries. We instead derive the analytical warp field of Gaussians to refine geometries and motions.

warp field, often referred to as a forward warp field due to its function of warping the canonical representation forward to a specific point in time. This warp field is typically modeled using learnable Multi-Layer Perceptrons (MLPs) or offset values, as seen in frameworks like DeformableGS [8] and Dynamic-GS [9]. These approaches have laid the groundwork for dynamic Gaussian scene modeling.

The community has explored structural cues such as optical flow and monocular depth to help regulate the temporal transitions of Gaussians. However, enforcing structural constraints with respect to a generic forward warp field as in the DeformableGS [8] is non-trivial. Intuitively, scene flows can be computed by forward warping of canonical scenes towards two queried frames, then evaluating the travelled trajectories. This approach is problematic since it relies on accurate structural priors, which are often unavailable for monocular casual sequences. Performing time-integration on an auxiliary network predicting the velocity field will introduce computational overhead and is theoretically unconstrained. Counter to the data-driven approach, we show that we can actually derive velocity fields directly from a generic warp field tailoring Lucas-Kanade for Gaussian Splatting, which can then be time-integrated for structural comparisons. Regulating the Gaussian motions through analytical velocity fields addresses the deficiencies of data-driven structural regularizations, as it promotes warp field learning on a continuous time domain without introducing additional learnable parameters.

In real-world captures, our approach outperforms state-of-the-art methods, including other dynamic Gaussian techniques. We demonstrate that our warp field regularization accommodates deformations in complex scenes with minimal camera movement, achieving results competitive with NeRF frameworks and enabling Gaussian splatting to model highly dynamic scenes from static cameras. To summarize, our approach offers two key advantages:

Reduced Bias: Methods relying solely on data-driven learning of warp fields can be biased towards the visible time steps, neglecting the overall movement of Gaussians. Our method, applicable to forward warp field techniques, ensures accurate Gaussian trajectories throughout the sequence.

Improved Tractability: The derived analytical solution for warp field velocities provides greater tractability compared to directly supervising the flow field as the difference in estimated deformations between consecutive frames.

2 Related Works

Neural Radiance Fields (NeRFs). NeRFs [10] have demonstrated exceptional capabilities in synthesizing novel views of static scenes. Their approach uses a fully-connected deep network to represent a scene’s radiance and density. Since its introduction, NeRF has been extended to dynamic scenarios by several works [11, 12, 13, 14, 15, 16]. Some of these methods leverage rigid body motion fields [12, 13] while others incorporate translational deformation fields with temporal positional encoding [14, 15]. Despite the advantages of NeRF and its dynamic extensions, they often impose high computational demands for both training and rendering.

Gaussian Splatting. The computational complexity of Neural Radiance Fields (NeRF) has spurred the development of alternative 3D scene representation methods. 3D Gaussian Splatting (3DGS)

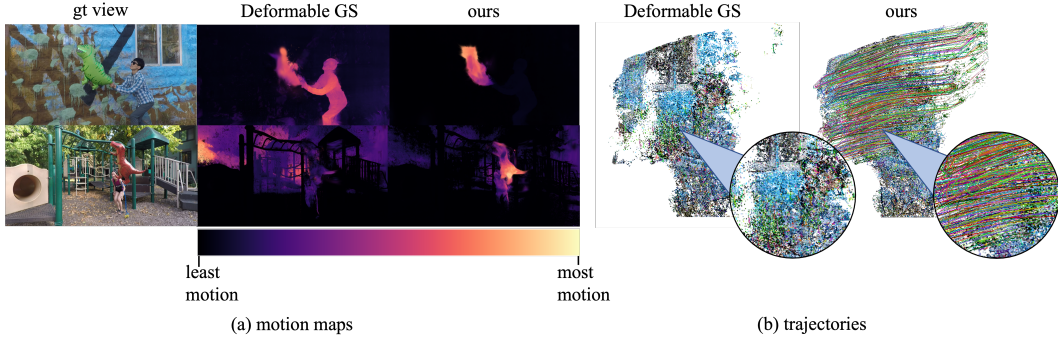


Figure 2: (a) Visualization of Gaussians’ travel distance $\|\mathbf{p} - \mathbf{p}_o\|_2$. For both of the scenes, the humans are stationary with dinosaur balloons moving around. Our result correctly identifies the dynamic regions, whereas the baseline model forms motions in the background and on supposedly stationary humans to compensate for photometric correctness. (b) 3D visualization of the motion trajectories. Our result shows clean trajectories from the waving balloon.

[6] has emerged as a promising solution, leveraging 3D Gaussians to model scenes and offering significant advantages over NeRF in terms of rendering speed and training efficiency.

While initially focused on static scenes, recent works [8, 17] have extended 3DGS to the dynamic domain. These approaches introduce a forward warp field that maps canonical Gaussians to their corresponding spacetime locations, enabling the representation of dynamic scene content. DeformableGS [8] employs an MLP to learn positional, rotational, and scaling offsets for each Gaussian, creating an over-parameterized warp field that captures complex spacetime relationships. 4DGaussians [17] further refine this approach by leveraging hexplane encoding [18, 19] to connect adjacent Gaussians. DynamicGS [9] incrementally deforms Gaussians along the tracked time frame. Despite these advancements, existing dynamic 3DGS methods struggle with highly dynamic scenes and near-static camera viewpoints. To overcome these limitations, we propose a novel approach that grounds the warp field directly on approximated scene flow.

Flow supervision. Optical flow supervision has been widely adopted for novel view synthesis and 3D reconstruction. Dynamic NeRFs [5, 20, 21, 22, 23, 4] have explored implicit scene flow representation with an Invertible Neural Network, semi-explicit representation from time integrating a learned velocity field, and explicit analytical derivation from the deformable warp field.

Several Gaussian Splatting works have begun exploring flow supervision. Motion-aware GS [24] applies flow supervision on the cross-dimensionally matched Gaussians from adjacent frames, without explicitly accounting for the flow contributions of Gaussians to each queried pixel. Gao et al.[25] on avatar rendering apply flow supervision for adjacent frames after rendering the optical flow map with α -blending [26]. This work regularizes the warp field through data-driven flow supervision, which is only suitable for enforcing short-term geometric consistency but becomes intractable for out-of-distribution time steps [27, 28]. In the context of dynamic Gaussian Splatting, we propose to regularize the deformable warp field through analytical time integration to ensure geometric consistencies.

3 Preliminary

Dynamic Gaussian Splatting. Dynamic 3D Gaussian Splatting frameworks follow a similar optimization pipeline as static Gaussian Splatting. Each Gaussian is defined by parameters for its mean μ , covariance Σ , and spherical harmonics SH color coefficients. To project Gaussians from 3D to 2D, we calculate the view space covariance matrix as follows:

$$\Sigma' = \mathbf{J}\mathbf{W}\Sigma\mathbf{W}^T\mathbf{J}^T, \quad (1)$$

where \mathbf{J} is the Jacobian of the projective transformation and \mathbf{W} is the viewing transform. To represent a scene’s radiance, the covariance Σ is decomposed into scaling matrices \mathbf{S} and rotation matrices \mathbf{R} as: $\Sigma = \mathbf{R}\mathbf{S}\mathbf{S}^T\mathbf{R}^T$. This decomposition supports differential optimization for dynamic Gaussian

Splatting. The color C is derived using a NeRF-like volumetric rendering equation:

$$\mathbf{C} = \sum_{i=1}^N T_i (1 - \exp(-\sigma_i \delta_i)) \mathbf{c}_i \quad \text{with} \quad T_i = \exp\left(-\sum_{j=1}^{i-1} \sigma_j \delta_j\right). \quad (2)$$

Adaptive density control manages the density of 3D Gaussians, allowing dynamic variation over iterations. For more details, refer to [6].

Dynamic Gaussian Splatting frameworks maintain a canonical space and learn warp fields \mathcal{F} that transform canonical Gaussians \mathcal{G} to the deformed space at time t :

$$\delta\mathcal{G} = \mathcal{F}_\theta(\mathcal{G}, t). \quad (3)$$

Following deformation, a novel-view image \hat{I} is rendered using differential rasterization [6] with a view matrix $M = [R, T]$ and target time t . While MLP-based deformation mapping often suffers from overfitting to training views, leading to degraded novel-view reconstruction, we address this by enforcing analytical constraints on the warp field. This ensures Gaussian motions adhere to the expected scene flow field, mitigating the issues of overfitting and SfM-initialized point cloud limitations.

Warp Field with twist increments. Let $P_\tau \in \mathbb{R}^{N_1 \times 3}$ and $P_s \in \mathbb{R}^{N_2 \times 3}$ be the target and source point clouds respectively, where N denotes the number of points respectively. The warp field that defines the rigid transformation that aligns the source point cloud to the template point cloud in the special Euclidean group can be expressed as $\mathcal{W}(\xi) = \exp(\sum_{p=1}^6 \xi_p \mathbf{T}_p) \in SE(3)$. The twist parameters in exponential mapping are the $\xi \in \mathbb{R}^6$, and the generator matrices are \mathbf{T} . The warp field can be optimized by minimizing the differences between the source and the target point clouds as:

$$\operatorname{argmin}_\xi \|\phi(\mathcal{W}(\xi) \cdot P_s) - \phi(P_\tau)\|_2^2, \quad (4)$$

where $\phi: \mathbb{R}^{N \times 3} \rightarrow \mathbb{R}^K$ is an encoding function that either explicitly extracts geometric features such as edges and normals, or implicitly encodes the point clouds into feature vectors. The (\cdot) denotes the warp field transformation. The optimization of the warp field incrementally learns the twist parameter as $\Delta\xi$ that best aligns the encoded source point cloud to the target point cloud.

This optimization can be solved iteratively given the twist parameter Jacobian matrix \mathbf{J} that can be further decomposed into a product of warp field gradient and the encoding functional gradient as:

$$\mathbf{J} = \frac{(\mathcal{W}^{-1}(\xi) \cdot P_\tau)}{\partial \xi^T} \cdot \frac{\partial \phi(\mathcal{W}^{-1}(\xi) \cdot P_\tau)}{\partial (\mathcal{W}^{-1}(\xi) \cdot P_\tau)^T}. \quad (5)$$

The transformations are applied iteratively until convergence.

4 Gaussian Splatting warp field regularization by scene flow

We study the problem of fitting deformable Gaussian Splatting from a monocular video sequence. Using structure-from-motion methods, we initialize the canonical Gaussians and camera parameters. For a given 3D Gaussian set \mathcal{G} at time t , the warp field deforms the Gaussians from canonical space to their positions at time t . We seek the optimal network parameters θ for the forward warp field $\mathcal{W}_{c \rightarrow t}$ so that the scene flow mapping $\mathcal{T}_{t \rightarrow t+1}$ and the rasterized image $\hat{\mathcal{I}}_t$ match the expected flow field and input image \mathcal{I}_t :

$$\operatorname{argmin}_\theta \Sigma_t \left[\sum_{t' \in \{t \pm \Delta t\}} \|(\hat{\mathcal{T}}_{t \rightarrow t+1} - \mathcal{T}_{t \rightarrow t+1})\|_p + \|\hat{\mathcal{I}}_t - \mathcal{I}_t\|_2^2 \right]. \quad (6)$$

The scene flow can be further decomposed into optical flow and depth estimations corresponding to the in-plane and out-of-plane motions. Suppose a point $\mathbf{p} = \mathbf{p}(t)$ moves in the scene. The projected location of this point from a static viewpoint camera i is $\mathbf{u}_i = \mathbf{u}_i(t)$, with \mathbf{u}_i 's change rate with respect to time as $\frac{d\mathbf{u}_i}{dt} = \frac{\partial \mathbf{u}_i}{\partial \mathbf{p}} \frac{d\mathbf{p}}{dt}$. Although the mapping from image coordinates to the scene coordinates is not unique, the relationship between \mathbf{p} and \mathbf{u}_i can be loosely expressed with dependencies on time as $\mathbf{p} = \mathbf{p}(\mathbf{u}_i(t); t)$ [29]. Now differentiating this mapping expression to time gives:

$$\frac{d\mathbf{p}}{dt} = \frac{\partial \mathbf{p}}{\partial \mathbf{u}_i} \frac{d\mathbf{u}_i}{dt} + \frac{d\mathbf{p}}{dt} \Big|_{\mathbf{u}_i}. \quad (7)$$

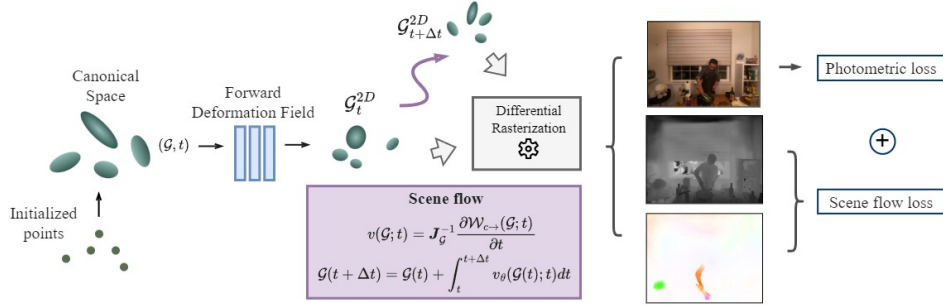


Figure 3: **Analytical scene flow from warp field.** With canonical Gaussians \mathcal{G}_c , we transform them forward in time to \mathcal{G}_t , then perform time integration from warp field velocities $v(\mathcal{G}; t)$ to derive $\mathcal{G}_{t+\Delta t}$. The Gaussian offsets $\mathcal{G}_{t+\Delta t} - \mathcal{G}_t$ are compared to reference scene flow.

This describes the motion of a point in 3D space using the scene flow projection on the image plane and the out-of-plane scene flow component. The in-plane component, $\frac{du_i}{dt}$, is obtained by projecting the instantaneous motion on the image plane, and the out-of-plane term represents the motion along \mathbf{u}_i 's corresponding ray. This decouples regularization on the optical flow field and the depth field from the estimated scene flow. The scene flow regularization then becomes:

$$\mathcal{L}_{scene} = \|(\hat{\mathcal{T}}_{t \rightarrow t+1} - \mathcal{T}_{t \rightarrow t+1})\|_p = \alpha \mathcal{L}_{o_{t \rightarrow t+1}} + \beta \mathcal{L}_{d_{t \rightarrow t+1}} \quad (8)$$

Decoupling the motions alleviates constraints on the supervision dataset and adds flexibility to the optimization. The regularization pipeline is visualized in Fig. 3. Implementation details are provided in Appendix A.1.

4.1 Forward warp field velocity

With the aforementioned problem statement, we show that the velocity field can be derived from the forward warp field. Restating the objective, we seek to find a warp field \mathcal{W} that transforms the canonical Gaussians \mathcal{G} forward in time such that it minimizes the appearance loss and scene flow loss at the target time step. To do this, we derive the velocity of the forward warp field as analogous to the twist Jacobians. The velocity field $v(\mathcal{G}; t)$ expresses the changes in Gaussian parameters in the world coordinate at a given time t . Gaussian Splatting maintains an explicit canonical Gaussian space so intuitively the velocities can be computed from its forward warp field $\mathcal{W}_{c \rightarrow}(\mathcal{G}, t)$ as:

$$v(\mathcal{G}; t) = \left. \frac{\partial \mathcal{W}_{c \rightarrow}(\mathcal{G}, t)}{\partial t} \right|_{(\mathcal{W}_{c \leftarrow}(\mathcal{G}, t); t)}. \quad (9)$$

The explicit expression of 3D Gaussians ensures that the scene flow mapping between the adjacent frames is bijective. In other words, the resulting correspondences among the 3D points in each frame are cyclic consistent since they are deformed from the same canonical Gaussian. This allows us to analytically compute the velocity field $v(\mathcal{G}; t)$ for each Gaussian in the canonical space.

The velocity field $v(\mathcal{G}; t)$ requires an analytical representation of the warp field's gradient concerning time and warp parameters. Although the direct analytical solution is costly to compute, the chain rule can be applied to decompose the compute into two partial terms: the feature gradient of the warp field with respect to the corresponding Gaussian parameter, and the analytical warp Jacobian [27, 30]:

$$v(\mathcal{G}; t) = \mathbf{J}_{\mathcal{G}}^{-1} \frac{\partial \mathcal{W}_{c \rightarrow}(\mathcal{G}; t)}{\partial t} = \frac{\partial \mathcal{W}_{c \rightarrow}(\mathcal{G}; t)}{\partial \mathcal{G}} \frac{\partial \mathcal{W}_{c \rightarrow}(\mathcal{G}; t)}{\partial t}. \quad (10)$$

The warp field feature gradient $\frac{\partial \mathcal{W}_{c \rightarrow}(\mathcal{G}; t)}{\partial t}$ describes how each output Gaussian parameter offsets changes with respect to the input canonical Gaussian parameters. The warp Jacobian $\frac{\partial \mathcal{W}_{c \rightarrow}(\mathcal{G}; t)}{\partial \mathcal{G}}$ describes how changes in the warp field output affect the transformation on the Gaussians.

We note that the expression holds for any Gaussian parameter that is an input to the deformation network $\mathcal{W}_{c \rightarrow}$ as long as the respective input and output dimensions are the same. However, in practice, the warp Jacobian can experience numerical instabilities with $\det(\mathbf{J}_{\mathcal{G}}) < \epsilon$, especially when

the canonical Gaussian scene has not stabilized. However, discarding unstable motions also affects the downstream densification and pruning process. We instead replace \mathbf{J}_G^{-1} with Moore–Penrose pseudoinverse operation \mathbf{J}_G^+ . The scaling terms and spherical harmonics of Gaussians have minimal changes between adjacent frames, we thus choose to exclude them from the compute for efficiency. Overall, we compute the velocity fields for Gaussians’ displacement and rotation as:

$$v(\mathbf{p}; t) = \mathbf{J}_p^+ \frac{\partial \mathcal{W}_{c \rightarrow}(\mathbf{p}; t)}{\partial t}; v(\mathbf{q}; t) = \mathbf{J}_q^+ \frac{\partial \mathcal{W}_{c \rightarrow}(\mathbf{q}; t)}{\partial t}, \quad (11)$$

where $v(\mathbf{p}; t) : \mathbb{R}^3 \times \mathbb{R} \rightarrow \mathbb{R}^3$ and $v(\mathbf{q}; t) : \mathbb{R}^4 \times \mathbb{R} \rightarrow \mathbb{R}^4$ respectively describes the positional and rotational velocity of a Gaussian in the world coordinate.

4.2 Scene field from time integration

Time integration on velocity field. Given the velocity field from equation 10, and 3D Gaussians $\mathcal{G}(t)$ observed at time step t , we can apply time integration using a Runge-Kutta [31] numerical solver on the velocity field to obtain the offset parameters for Gaussians at time $(t + \Delta t)$:

$$\mathcal{G}(t + \Delta t) = \mathcal{G}(t) + \int_t^{t+\Delta t} v_\theta(\mathcal{G}(t); t) dt. \quad (12)$$

We then train the warp field network to minimize the difference between the predicted scene flow derived from the analytical velocity field, and the ground truth scene flow decomposed into optical flow and depth describing the in-plane and out-of-plane Gaussian motions.

Optical flow and depth rendering from Gaussians. For each Gaussian at time t , we compute each of the corresponding positions and rotations at $(t + \Delta t)$. For rendering the optical flow and depth map, we consider the full freedom of each Gaussian motion.

For optical flow rendering, we want to calculate the motion’s influence on pixel shifts from all Gaussians in the world coordinate. In the original 3D Gaussian Splatting, a pixel’s color is the weighted sum of the projected 2D Gaussian’s radiance contribution. Analogous to this formulation, the optical flow at a queried pixel is the weighted sum of the 2D Gaussians’ contribution to the pixel shift:

$$\hat{flow}_{t,t+\Delta t}^G = \sum_{i \in N} flow_i \alpha_i \prod_{j=1}^{i-1} (1 - \alpha_j) = \sum_{i=1} w_i [\sum_{i,t_2} \sum_{i,t_1}^{-1} (x_{t_1} - \mu_{i,t_1}) + \mu_{i,t_2} - x_{t_1}], \quad (13)$$

where $flow_i$ denotes the optical flow of Gaussian \mathcal{G}_i , and $w_i = \frac{T_i \alpha_i}{\sum_i T_i \alpha_i}$ denotes the weighing factor of each Gaussian from α -blending.

Similarly, the per-pixel z-depth estimates \hat{d} can be rendered from the discrete volume rendering approximation accounting for the per-Gaussian contributions:

$$\hat{D}_{t,t+\Delta t}^G = \sum_{i \in N} d_i \alpha_i \prod_{j=1}^{i-1} (1 - \alpha_j), \quad (14)$$

where d_i denotes the z-depth value of Gaussian \mathcal{G}_i from the viewing space. We normalize the optical flow and depth estimates for numerical stability. The optical flow and depth maps are rasterized simultaneously in the same forward pass with color.

5 Experiments

In this section, we first provide the implementation details of the proposed warp field regulation and then validate our proposed method on four dynamic scene datasets captured with different levels of camera movements. We showcase the quantitative and qualitative results of the Dynamic Scenes dataset [32], Planoptic Video dataset [33], HyperNeRF dataset [13], and DAVIS dataset [34]. Our method achieves state-of-the-art results on both static and dynamic cameras.

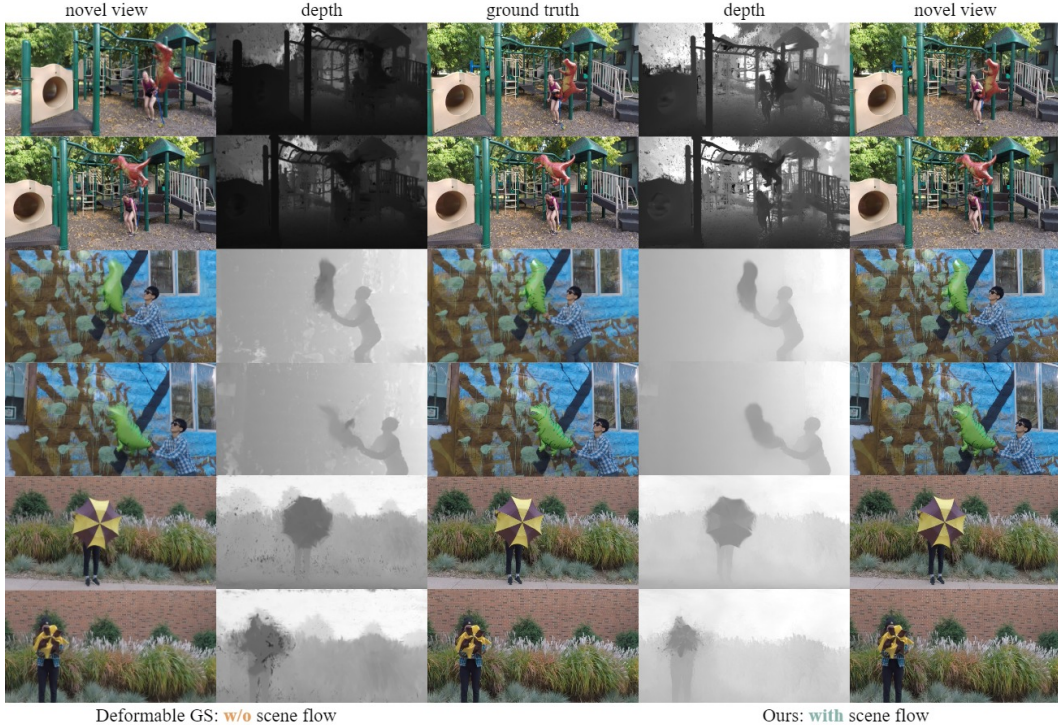


Figure 4: **Qualitative comparisons on the Dynamic Scenes dataset.** Compared to the baseline method, our approach can achieve superior rendering quality on real datasets with lower EMFs.

5.1 Implementation details

We implement the warp field using PyTorch [35], leveraging its `Autodiff` library for gradient and Jacobian computations. The framework is optimized with Adam [36] as with 3DGS [6] on a NVIDIA A100 Tensor Core [37]. We use the `TorchdiffEq` [38] library for numerical integration. Modified from DeformableGS, the inputs to the warp field include 3D Gaussian positions (\mathbf{p}), time (t), and 3D Gaussian rotations (\mathbf{q}) in quaternions. Velocity derivations are enabled by removing the stop gradient operation from the network inputs. Positional encoding [3] is applied to extend inputs’ frequency band [39]. We refer readers to Appendix A.2 for more implementation details.

5.2 Evaluation

Here we analyze the performance of our method quantitatively and qualitatively. We aim to study if the analytical scene flow regularization on the warp field helps disambiguate the dynamic scene geometry and promote the reconstruction of low EMF scenes.

Benchmarked datasets. We evaluate our method using real-world monocular datasets with varying camera motion. These include Dynamic Scene [32], captured by a stationary multi-view 8 camera rig with significant scene motion; Plenoptic Video [33], captured using a static rig with 21 GoPro cameras [40]; Hypernerf [13], which captures objects with moving topologies from a moving camera, suitable for quasi-static reconstruction; and sequences from DAVIS 2017 [34] dataset containing near-static monocular videos.

Quantitative baseline comparisons. We evaluate our method’s novel-view synthesis capabilities on three datasets: Plenoptic Videos, Hypernerf, and Dynamic Scenes, ordered by decreasing Effective Multi-view Factor (EMF) [1]. These datasets present increasing challenges, with Dynamic Scenes posing the greatest difficulty due to its low EMF and unreliable object motion. We assess visual quality using LPIPS [41], SSIM [42], and PSNR [43], comparing our method to static Gaussian Splatting [6], DeformableGS [8], and 4DGaussians [17], as shown in Table 3 and Table 2. Our method consistently outperforms these baselines on scenes with higher EMFs (Plenoptic Videos and

Table 1: **Quantitative evaluation of novel view synthesis on the Dynamic Scenes dataset.** See Sec. 5.2 for descriptions of the baselines.

method	Playground			Balloon1			Balloon2			Umbrella		
	PSNR \uparrow	SSIM \uparrow	LPIPS \downarrow	PSNR \uparrow	SSIM \uparrow	LPIPS \downarrow	PSNR \uparrow	SSIM \uparrow	LPIPS \downarrow	PSNR \uparrow	SSIM \uparrow	LPIPS \downarrow
NSFF	24.69	0.889	0.065	24.36	0.891	0.061	30.59	0.953	0.030	24.40	0.847	0.088
NR-NeRF	14.16	0.337	0.363	15.98	0.444	0.277	20.49	0.731	0.348	20.20	0.526	0.315
Nerfies (w flow)	22.18	0.802	0.133	23.36	0.852	0.102	24.91	0.864	0.089	24.29	0.803	0.169
Flow-sup. NeRF	22.39	0.812	0.109	24.36	0.865	0.107	25.82	0.899	0.081	24.25	0.813	0.123
	16.70	0.597	0.168	19.53	0.654	0.175	20.13	0.719	0.113	18.00	0.597	0.148
Deformable GS	<u>24.82</u>	0.646	0.343	22.40	0.833	<u>0.137</u>	<u>24.19</u>	<u>0.818</u>	<u>0.153</u>	<u>22.35</u>	<u>0.711</u>	<u>0.186</u>
4DGaussians	21.39	0.776	<u>0.204</u>	<u>24.48</u>	0.849	0.144	24.72	0.801	0.219	21.29	0.560	0.332
Ours	26.34	<u>0.756</u>	0.184	26.35	<u>0.848</u>	0.133	25.89	0.911	0.151	23.02	0.746	0.176

Hypernerf). To further assess our method’s performance, we compare its novel-view synthesis results with NSFF [5], NR-NeRF [15], Nerfies [12], and Flow-supervised NeRF [30] on the Dynamic Scenes dataset, see Table 1. These comparisons highlight the effectiveness of our analytical scene flow approach compared to other flow-guided rendering frameworks. Notably, our method outperforms NSFF, which uses a similar supervision style but a different scene flow derivation. The comparison with Flow-supervised NeRF, which also uses analytical scene flow derived from an implicit radiance field, serves as an ablation study, demonstrating the effectiveness of our derived scene flow on an explicit scene representation. Finally, we support the aforementioned decomposed structural supervision as in Table 4. More discussions on alternative setups are provided in Appendix Sec. A.3.

Table 2: **Quantitative evaluation of novel view synthesis on the Plenoptic Videos dataset.** See Sec 5.2 for an analysis of the performance.

method	cook spinach			cut roasted beef			sear steak			Mean		
	PSNR \uparrow	SSIM \uparrow	LPIPS \downarrow	PSNR \uparrow	SSIM \uparrow	LPIPS \downarrow	PSNR \uparrow	SSIM \uparrow	LPIPS \downarrow	PSNR \uparrow	SSIM \uparrow	LPIPS \downarrow
Deformable GS	<u>32.97</u>	<u>0.947</u>	0.087	30.72	<u>0.941</u>	0.090	<u>33.68</u>	<u>0.955</u>	0.079	<u>32.46</u>	<u>0.948</u>	0.085
4DGaussians	31.98	0.938	0.056	<u>31.56</u>	0.939	0.062	31.20	0.949	0.045	31.58	0.942	0.055
Ours	33.91	0.951	<u>0.064</u>	32.40	0.957	<u>0.084</u>	34.02	0.963	<u>0.057</u>	33.44	0.954	<u>0.068</u>

Table 3: **Quantitative evaluation on the Hypernerf dataset.** See Sec. 5.2 for detailed explanations.

method	PSNR \uparrow	SSIM \uparrow	LPIPS \downarrow
3DGS	20.84	0.70	0.45
Deformable GS	26.47	<u>0.79</u>	<u>0.29</u>
4DGaussians	<u>26.98</u>	0.78	0.31
Ours	27.38	0.81	0.26

Table 4: **Ablation study on scene flow decomposition on "Playground" scene from Dynamic Scenes dataset.** See Sec. 5.2 for detailed descriptions of each ablated design.

method	PSNR \uparrow	SSIM \uparrow	LPIPS \downarrow
w/ Depth Sup.	24.76	0.711	0.274
w/ Flow Sup.	24.37	0.695	0.229
Ours	26.34	0.756	0.184

Trajectories from scene flow fields. We visualize the scene flow trajectories from Dynamic Scenes Dataset sequences to assess the quality and smoothness of the derived flow field. The Gaussians are subsampled from the dynamic regions of the canonical Gaussian space, and then time integrated to produce their respective displacements across time, visualized as colored trajectories in Fig. 2. We note that the trajectories are smooth and follow the expected motions of the dynamic objects. The visualized trajectories of the sequences demonstrate the framework’s potential to be extended for tracking in dynamic 3D Gaussian scenes. More trajectories on the DAVIS dataset will be shown in the appendix.

Geometric consistency. Fig. 4 compares our method with DeformableGS, which learns Gaussians’ time dependency without scene flow regularization. While DeformableGS renders visually accurate novel views, the underlying scene structures are inaccurate, leading to blurry dynamic objects and artifacts in depth maps. Our method, leveraging analytical scene flow regularization, achieves more accurate geometries, reflected in both visual and quantitative results (Table 1). This also enables accurate Gaussian motion tracking (Fig. 2). To explore alternative design choices, we compare with direct flow and depth supervision on DeformableGS (Fig. 1). These comparisons indicate that our approach, which enforces regularization on the expected scene flow over a continuous time frame, results in more plausible scene structures compared to discrete time step supervision.

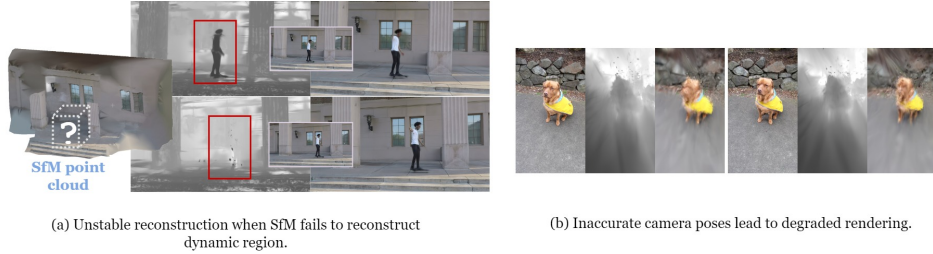


Figure 5: Our method struggles with insufficient point cloud initialization due to reliance on non-rigid warping of scene geometry. In the ‘skating’ scene, this results in unstable geometry at certain angles. Inaccurate camera calibrations also degrade our method, as shown in the ‘toby-sit’ sequence, where miscalibration distorts the scene geometry.

Static and dynamic motion separation. Our approach formulates deformations within a canonical Gaussian space. To assess the fidelity of our method in separating static and dynamic regions, we visualize the travel distance of each Gaussian from its canonical projection to a queried viewing camera in Fig. 2. The plots are color-coded by the absolute travel distance, with yellow indicating larger distances and purple indicating smaller distances.

In the Playground scene featuring human-object interactions, the visualized travel distance is greatest at the far-side boundaries of the moving object as it recedes from the human. The scene’s background is correctly rendered as static with minimal motion. This visualization demonstrates the effectiveness of our method in accurately identifying dynamic regions. Moreover, these results suggest promising future directions for optimizing dynamic scene rendering by filtering out static regions from the optimization process, potentially reducing computational costs.

6 Limitations

Sensitivity to SfM Initialization: Our approach is sensitive to the quality of the Structure-from-Motion (SfM) Gaussian space initialization. Accurate initialization is crucial for 3D Gaussian Splatting, particularly without other scene priors. As shown in Fig. 5.a, reconstruction quality deteriorates when dynamic regions have insufficient initialized points.

Camera Parameter Sensitivity: Our method is sensitive to inaccuracies in bundle-adjusted camera intrinsic and extrinsic parameters. Errors in these parameters lead to inaccurate rasterization projections, causing noisy geometry or failed reconstruction, as shown in Fig. 5.b.

Computational Complexity: The pseudo-inverse operation for velocity field computation requires $(N \times d)$ square matrix decompositions, where N is the number of Gaussians, and d is the number of Gaussian parameters. Potential mitigations include optimized implementations or pre-filtering to remove static Gaussians.

7 Conclusion

This paper presents a method for incorporating scene flow regularization into deformable Gaussian Splatting. We derive an analytical scene flow representation, drawing upon the theoretical foundations of rigid transformation warp fields in point cloud registration. Our approach significantly enhances the structural fidelity of the underlying dynamic Gaussian geometry, enabling reconstructions of scenes with rapid motions.

Comparison with other Deformable Gaussian Splatting variants demonstrates that regularizing on the warp-field derived scene flow produces more accurate dynamic object geometries and improved motion separation due to its continuous-time regularization. Additionally, comparison with flow-supervised NeRFs reveals the advantages of using Gaussians’ explicit scene representations.

While our method exhibits limitations as discussed in the previous section, the accurate geometries learned from dynamic scenes open up promising possibilities for future applications, including 3D tracking from casual hand-held device captures and in-the-wild dynamic scene rendering.

References

- [1] H. Gao, R. Li, S. Tulsiani, B. Russell, and A. Kanazawa, “Monocular dynamic view synthesis: A reality check,” in *Advances in Neural Information Processing Systems* (S. Koyejo, S. Mohamed, A. Agarwal, D. Belgrave, K. Cho, and A. Oh, eds.), vol. 35, pp. 33768–33780, Curran Associates, Inc., 2022.
- [2] J. L. Schönberger and J.-M. Frahm, “Structure-from-Motion Revisited,” in *Conference on Computer Vision and Pattern Recognition (CVPR)*, 2016.
- [3] B. Mildenhall, P. P. Srinivasan, M. Tancik, J. T. Barron, R. Ramamoorthi, and R. Ng, “Nerf: representing scenes as neural radiance fields for view synthesis,” *Commun. ACM*, vol. 65, p. 99–106, dec 2021.
- [4] S. Chen, B. Yan, X. Sang, D. Chen, P. Wang, X. Guo, C. Zhong, and H. Wan, “Bidirectional Optical Flow NeRF: High Accuracy and High Quality under Fewer Views,” in *Proceedings of the 37th AAAI Conference on Artificial Intelligence, AAAI 2023*, vol. 37, 2023.
- [5] Z. Li, S. Niklaus, N. Snavely, and O. Wang, “Neural Scene Flow Fields for Space-Time View Synthesis of Dynamic Scenes,” in *Proceedings of the IEEE Computer Society Conference on Computer Vision and Pattern Recognition*, 2021.
- [6] B. Kerbl, G. Kopanas, T. Leimkühler, and G. Drettakis, “3d gaussian splatting for real-time radiance field rendering,” *ACM Transactions on Graphics (ToG)*, vol. 42, no. 4, pp. 1–14, 2023.
- [7] N. Micheletti, J. H. Chandler, and S. N. Lane, “Structure from Motion (SfM) Photogrammetry,” *British Society for Geomorphology Geomorphological Techniques*, vol. 2, no. 2, pp. 1–12, 2015.
- [8] Z. Yang, X. Gao, W. Zhou, S. Jiao, Y. Zhang, and X. Jin, “Deformable 3D Gaussians for High-Fidelity Monocular Dynamic Scene Reconstruction,” 9 2023.
- [9] J. Luiten, G. Kopanas, B. Leibe, and D. Ramanan, “Dynamic 3d gaussians: Tracking by persistent dynamic view synthesis,” in *3DV*, 2024.
- [10] B. Mildenhall, P. P. Srinivasan, M. Tancik, J. T. Barron, R. Ramamoorthi, *et al.*, “NeRF: Representing Scenes as Neural Radiance Fields for View Synthesis,” *Commun. ACM*, vol. 65, no. 1, pp. 99–106, 2021.
- [11] G. Gafni, J. Thies, M. Zollhofer, and M. Nießner, “Dynamic Neural Radiance Fields for Monocular 4D Facial Avatar Reconstruction,” in *Proc. IEEE/CVF CVPR*, pp. 8649–8658, 2021.
- [12] K. Park, U. Sinha, J. T. Barron, S. Bouaziz, D. B. Goldman, *et al.*, “Nerfies: Deformable Neural Radiance Fields,” in *Proc. IEEE/CVF ICCV*, pp. 5865–5874, 2021.
- [13] K. Park, U. Sinha, P. Hedman, J. T. Barron, S. Bouaziz, D. B. Goldman, R. Martin-Brualla, and S. M. Seitz, “HyperNeRF: A Higher-Dimensional Representation for Topologically Varying Neural Radiance Fields,” *ACM Transactions on Graphics*, vol. 40, no. 6, 2021.
- [14] A. Pumarola, E. Corona, G. Pons-Moll, and F. Moreno-Noguer, “D-NeRF: Neural Radiance Fields for Dynamic Scenes,” in *Proc. IEEE/CVF CVPR*, pp. 10318–10327, 2021.
- [15] E. Tretschk, A. Tewari, V. Golyanik, M. Zollhöfer, C. Lassner, *et al.*, “Non-Rigid Neural Radiance Fields: Reconstruction and Novel View Synthesis of a Dynamic Scene From Monocular Video,” in *Proc. IEEE/CVF ICCV*, pp. 12959–12970, 2021.
- [16] H. Yu, J. Julin, Z. A. Milacski, K. Niinuma, and L. A. Jeni, “Dylin: Making light field networks dynamic,” in *2023 IEEE/CVF Conference on Computer Vision and Pattern Recognition (CVPR)*, pp. 12397–12406, 2023.
- [17] G. Wu, T. Yi, J. Fang, L. Xie, X. Zhang, W. Wei, W. Liu, Q. Tian, and W. Xinggang, “4d gaussian splatting for real-time dynamic scene rendering,” *Proceedings of the IEEE/CVF Conference on Computer Vision and Pattern Recognition (CVPR)*, 2024.
- [18] J. Fang, T. Yi, X. Wang, L. Xie, X. Zhang, W. Liu, M. Nießner, and Q. Tian, “Fast dynamic radiance fields with time-aware neural voxels,” in *SIGGRAPH Asia 2022 Conference Papers*, 2022.
- [19] A. Cao and J. Johnson, “HexPlane: A Fast Representation for Dynamic Scenes,” 2023.
- [20] X. Li, J. Zheng, F. Ferroni, J. K. Pontes, and S. Lucey, “Fast Neural Scene Flow,” *Proceedings of the IEEE/CVF International Conference on Computer Vision (ICCV)*, pp. 9878–9890, 2023.
- [21] X. Li, J. K. Pontes, and S. Lucey, “Neural Scene Flow Prior,” in *Advances in Neural Information Processing Systems*, vol. 10, 2021.
- [22] E. Tretschk, A. Tewari, V. Golyanik, M. Zollhöfer, C. Lassner, and C. Theobalt, “Non-Rigid Neural Radiance Fields: Reconstruction and Novel View Synthesis of a Dynamic Scene From Monocular Video,” in *Proceedings of the IEEE International Conference on Computer Vision*, 2021.
- [23] C. Wang, L. E. MacDonald, L. A. Jeni, and S. Lucey, “Flow supervision for deformable nerf,” in *Proceedings of the IEEE/CVF Conference on Computer Vision and Pattern Recognition*, pp. 21128–21137, 2023.

- [24] Z. Guo, W. Zhou, L. Li, M. Wang, and H. Li, “Motion-aware 3D Gaussian Splatting for Efficient Dynamic Scene Reconstruction.” 3 2024.
- [25] Q. Gao, Q. Xu, Z. Cao, B. Mildenhall, W. Ma, L. Chen, D. Tang, and U. Neumann, “GaussianFlow: Splatting Gaussian Dynamics for 4D Content Creation,” 3 2024.
- [26] B. A. Wallace, “Merging and transformation of raster images for cartoon animation,” in *Proceedings of the 8th Annual Conference on Computer Graphics and Interactive Techniques, SIGGRAPH 1981*, 1981.
- [27] Y. Aoki, H. Goforth, R. A. Srivatsan, and S. Lucey, “Pointnetlk: Robust & efficient point cloud registration using pointnet,” in *Proceedings of the IEEE Computer Society Conference on Computer Vision and Pattern Recognition*, vol. 2019-June, 2019.
- [28] X. Li, J. K. Pontes, and S. Lucey, “PointNetlk revisited,” in *Proceedings of the IEEE Computer Society Conference on Computer Vision and Pattern Recognition*, 2021.
- [29] S. Vedula, P. Rander, R. Collins, and T. Kanade, “Three-dimensional scene flow,” *IEEE Transactions on Pattern Analysis and Machine Intelligence*, vol. 27, no. 3, pp. 475–480, 2005.
- [30] C. Wang, L. E. MacDonald, L. A. Jeni, and S. Lucey, “Flow supervision for deformable nerf,” in *Proceedings of the IEEE/CVF Conference on Computer Vision and Pattern Recognition (CVPR)*, pp. 21128–21137, June 2023.
- [31] E. Batschelet, “Über die numerische Auflösung von Randwertproblemen bei elliptischen partiellen Differentialgleichungen,” *ZAMP Zeitschrift für angewandte Mathematik und Physik*, vol. 3, no. 3, 1952.
- [32] J. S. Yoon, K. Kim, O. Gallo, H. S. Park, and J. Kautz, “Novel view synthesis of dynamic scenes with globally coherent depths from a monocular camera,” in *Proceedings of the IEEE Computer Society Conference on Computer Vision and Pattern Recognition*, 2020.
- [33] X. Li, J. K. Pontes, and S. Lucey, “Pointnetlk revisited,” in *Proceedings of the IEEE/CVF Conference on Computer Vision and Pattern Recognition (CVPR)*, pp. 12763–12772, June 2021.
- [34] F. Perazzi, J. Pont-Tuset, B. McWilliams, L. V. Gool, M. Gross, and A. Sorkine-Hornung, “A benchmark dataset and evaluation methodology for video object segmentation,” in *Proceedings of the IEEE Computer Society Conference on Computer Vision and Pattern Recognition*, vol. 2016-December, 2016.
- [35] A. Paszke, S. Gross, F. Massa, A. Lerer, J. Bradbury, G. Chanan, T. Killeen, Z. Lin, N. Gimelshein, L. Antiga, A. Desmaison, A. Köpf, E. Yang, Z. DeVito, M. Raison, A. Tejani, S. Chilamkurthy, B. Steiner, L. Fang, J. Bai, and S. Chintala, “PyTorch: An imperative style, high-performance deep learning library,” in *Advances in Neural Information Processing Systems*, vol. 32, 2019.
- [36] D. P. Kingma and J. L. Ba, “Adam: A method for stochastic optimization,” in *3rd International Conference on Learning Representations, ICLR 2015 - Conference Track Proceedings*, 2015.
- [37] Nvidia Corporation, “NVIDIA A100 Tensor Core,” 2024.
- [38] R. T. Q. Chen, “torchdiffq,” 2018.
- [39] J. Zheng, S. Ramasinghe, X. Li, and S. Lucey, “Trading positional complexity vs. deepness in coordinate networks,” *Proceedings of the European Conference on Computer Vision (ECCV)*, 2022.
- [40] I. GoPro, “Go Pro Hero 7,” 2023.
- [41] R. Zhang, P. Isola, A. A. Efros, E. Shechtman, and O. Wang, “The unreasonable effectiveness of deep features as a perceptual metric,” in *CVPR*, 2018.
- [42] Z. Wang, A. C. Bovik, H. R. Sheikh, and E. P. Simoncelli, “Image Quality Assessment: From Error Visibility to Structural Similarity,” *IEEE Trans. Image Process.*, vol. 13, no. 4, pp. 600–612, 2004.
- [43] S. Welstead, *Fractal and Wavelet Image Compression Techniques*. 2009.
- [44] Z. Teed and J. Deng, “Raft: Recurrent all-pairs field transforms for optical flow,” in *European Conference on Computer Vision*, 2020.
- [45] Guangcong, Z. Chen, C. C. Loy, and Z. Liu, “Sparsenerf: Distilling depth ranking for few-shot novel view synthesis,” *IEEE/CVF International Conference on Computer Vision (ICCV)*, 2023.
- [46] I. Epic Games, “Reality Capture,” 2024.
- [47] B. Ke, A. Obukhov, S. Huang, N. Metzger, R. C. Daudt, and K. Schindler, “Repurposing diffusion-based image generators for monocular depth estimation,” in *Proceedings of the IEEE/CVF Conference on Computer Vision and Pattern Recognition (CVPR)*, 2024.
- [48] Y. Du, Y. Zhang, H.-X. Yu, J. B. Tenenbaum, and J. Wu, “Neural radiance flow for 4d view synthesis and video processing,” in *2021 IEEE/CVF International Conference on Computer Vision (ICCV)*, pp. 14304–14314, IEEE Computer Society, 2021.

A Appendix / supplemental material

A.1 Scene Flow Regularization Formulation

Recall that in addition to the photometric regularization as detailed in the original 3D Gaussian Splatting [6], \mathcal{L}_{scene} is used as the structural regularization for the derived scene flow consisting of weighted depth and optical flow terms $\mathcal{L}_{scene} = \alpha\mathcal{L}_{o_{t \rightarrow t+1}} + \beta\mathcal{L}_{d_{t \rightarrow t+1}}$.

The optical flow term minimizes the absolute error between the rendered optical flow as computed from accounting for all Gaussians' 2D projected motion contributions to each rendered pixel, and the reference flow from RAFT [44]. In particular, the optical flow term is expressed as:

$$\mathcal{L}_{o_{t \rightarrow t+1}} = \frac{1}{n} \sum_{j=1}^n |o_j - \hat{o}_j|, \quad (15)$$

where j denotes the queried pixel from a rasterized image containing n total pixels.

As noted in SparseNeRF [45], monocular depth maps are scale-ambiguous thus directly using monocular depth priors with p -norm regularizations hinders the spatial coherency. We apply a local depth ranking loss on the rendered depth maps. We transfer the depth ranking knowledge from monocular depth d_{mono} to rendered d_r with:

$$\mathcal{L}_{d_{t \rightarrow t+1}} = \sum_{d_{mono}^{k_1} < d_{mono}^{k_2}} \max(d_r^{k_1} - d_r^{k_2} + m, 0), \quad (16)$$

where m is a tunable small margin defining the permissible depth ranking errors, and k_1, k_2 are the indices of the randomly queried pixels. If the depth ranking of the monocular depth pixels and the rendered pixels are not consistent, then it entails inaccuracies in the warped Gaussians at time $(t + \Delta t)$, penalizing the learned warp field.

The coefficients α and β reweight the magnitude of loss terms to compensate for regularizing with monocular depth cues. In practice, we notice that setting the two coefficients with similar magnitude yields satisfactory results for scenes initialized with dense point clouds. Whereas with insufficient SfM initialization, the motion coefficient α needs to be weighed down in earlier iterations to allow the canonical scene to stabilize.

A.2 Additional implementation Details

Scene initialization. We define the initialization stage as the first N iterations without deploying scene flow regularizations. To warm up the optimization, during the initialization stage, we only compute the photometric losses with the warp field network unfrozen. Note that we discarded the static scene initialization stage typically adopted by other dynamic Gaussian splatting frameworks as it provided incremental benefits.

The length of the warm-up period is defined based on the quality of the SfM scene. For scenes with rich point clouds to start with, we employ 3000 iterations for initialization to refine the canonical structures. Some highly dynamic scenes contain only a few points or no points in the dynamic regions. Since our method relies on analytical warping from the canonical scene and needs Gaussians at the dynamic regions to start with, we extend the warm-up period to 5000-10,000 to recover as many Gaussians as possible at the dynamic regions.

Motion masking. The initialized Gaussians generally carry inaccurate motions to compensate for photometric accuracies, regardless of whether the Gaussians are located at the presumably static or dynamic regions. Thus we first randomly sample pixels from the rendering to correct motions of all Gaussians equally across the scene. Since static regions are usually larger than dynamic regions and are easier to converge, this allows us to disambiguate the static and dynamic regions.

After ensuring that most Gaussians in the static regions have been sufficiently constrained, we apply a large motion mask to reconstruct small and fast-moving objects. The motion mask is defined similarly as prior work [5] as a binary segmentation mask at pixels with normalized motions larger than 0.1. This additional motion masking step allows us to focus on rapid motions when most of the scene motions have converged.

Training details. The hyperparameters for learning the Gaussian parameters are kept consistent as the original 3D Gaussian Splatting [6]. For comparable analysis on the analytical warp field regularization, we follow setups in the baselines [8, 17]. The learning rate of the warp field network is empirically set to decay from $8e-4$ to $1.6e-6$, and Adam’s β range is set to $(0.9, 0.999)$. As with data preparation, we used COLMAP [2] and Reality Capture [46] to estimate camera intrinsics and extrinsics, which are kept fixed during optimization. We use Marigold [47] and RAFT [44] for depth and flow maps.

A.3 Further Discussions on Motion Learning

Geometry enhances novel view reconstruction quality. Fig. 6 presents novel view synthesis results and learned geometries from our method alongside two baseline models. This comparison highlights the impact of accurate underlying geometries on synthesized novel views. All three models converge on the training views, so we focus on the results for unseen viewpoints. 4DGaussians [17] learns the

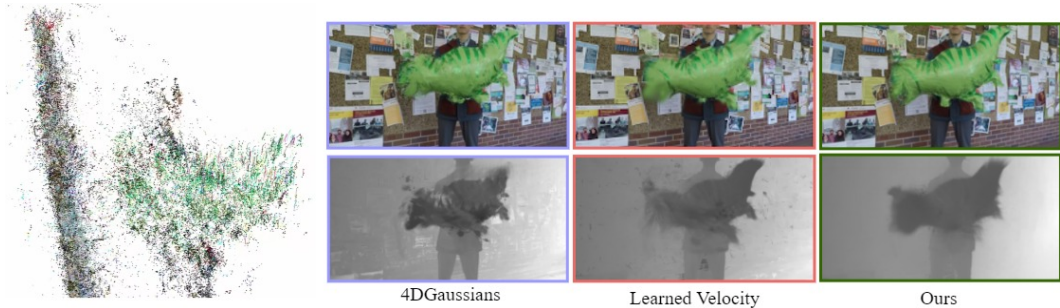


Figure 6: Visualization of Gaussian trajectories and comparison of novel view synthesis results with learned geometries.

warp field without incorporating motion cues. This approach leads to a noisy underlying geometry with artifacts around specular areas, likely introduced to compensate for photometric inaccuracies. Consequently, its synthesized dinosaur exhibits blurriness around the edges.

Another baseline predicts velocities directly instead of relying on analytical derivation as in Du et al. [48]. We adopt the velocity field model from Du et al. and perform time integration to derive scene flow. However, this data-driven velocity field tends to produce an "averaged" geometry, resulting in blurriness around the dinosaur’s head area.

In contrast, our method generates the most crisp depth map and the highest quality synthesized result. This improvement stems from our ability to accurately learn dynamic geometries. The left-hand side of the figure demonstrates that even with monocular sequences, our method effectively separates the foreground, background, and carried object. Our method serves as a general tool for enhancing dynamic Gaussian splatting frameworks without requiring additional network modules.

Motion thresholding visualizations. Fig. 7 presents a comparison of motion thresholds at different travel distances and our learned trajectories. The first row visualizes the 3D trajectories of Gaussians, color-coded by z-depth magnitude and in learned color. This visualization clearly demonstrates the accurate motions of a human waving a balloon. The second row displays the motion plot generated by our method, while the third row showcases the results from the DeformableGS baseline model [8]. The baseline model exhibits a significant error, moving the stationary human instead of the balloon. Notably, the side of the balloon furthest from the human experiences the least movement, while the human’s torso exhibits the most displacement. This outcome directly contradicts expectations. In contrast, our method accurately captures the motions, correctly ranking their magnitudes. This highlights the effectiveness of our approach in distinguishing and representing the dynamic elements within the scene.

Sensitivities to SfM initialization continued. As discussed in the limitations section, our method relies on analytical warping from canonical space, making it sensitive to Structure-from-Motion (SfM) initialization, particularly when dynamic regions lack sufficient point correspondences. Fig. 8 illustrates this sensitivity using the "train" scene from the DAVIS dataset [34]. The left side of the figure shows the SfM-initialized mesh, where the toy train traveling on the circular track is not

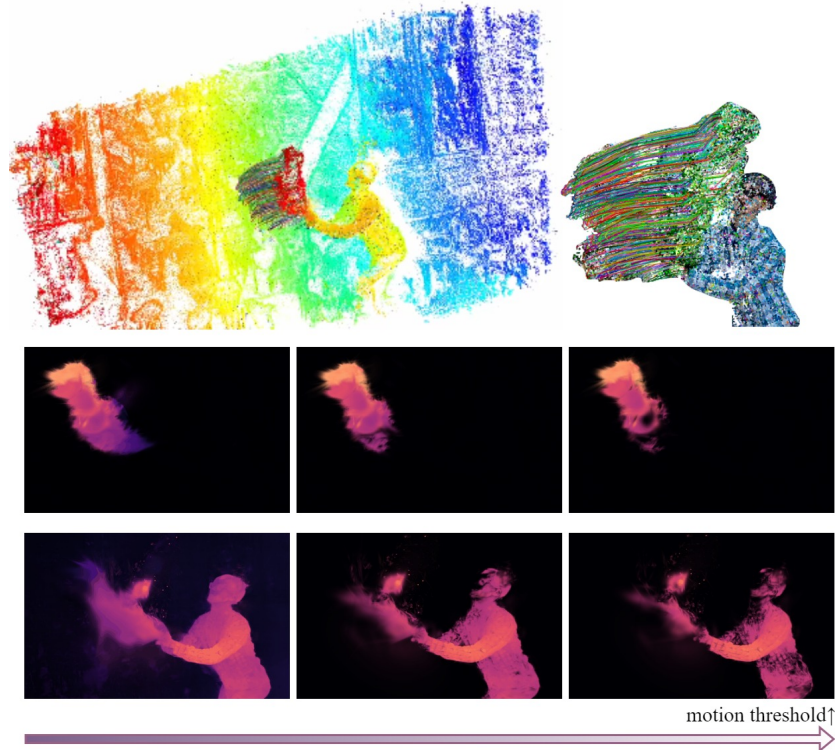


Figure 7: 3D trajectories and thresholded motion plots. The first row of motion plots are results from our method and the second row are results from baseline model DeformableGS.

captured. The top right figure displays the learned trajectories from the baseline model, exhibiting irregular Gaussian movements within the dynamic area.

The bottom right figure presents the learned trajectories from our method. While our method captures the expected trajectory of the moving train, it struggles to reconstruct dense Gaussians for the train due to an insufficient number of initialized Gaussians in this region. Additionally, the Gaussians are not accurately placed at the correct depth, as the monocular depth ranking loss only enforces the correct depth ranking order. Employing alternative depth regularization techniques could improve the learned depth in absolute scale.

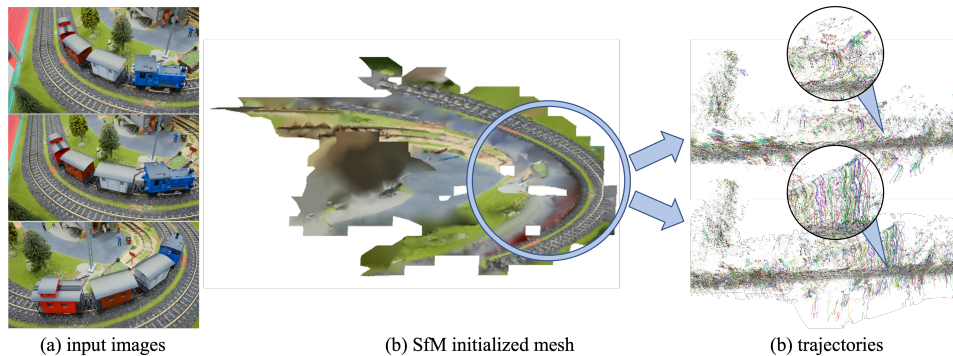


Figure 8: SfM initialized mesh and the reconstructed toy train trajectories. The right top subfigure shows trajectories from the baseline model, and the right bottom subfigure shows trajectories from our model.

More results on real scenes. More qualitative results on dynamic scenes can be found in Fig. 9.



(a) *Truck*



(b) *Skating*

Figure 9: Qualitative comparisons on Dynamic Scenes Dataset [32]